AIAA JOURNAL
Vol. 32, No. 8, August 1994

Velocity Field Imaging in Supersonic Reacting Flows near Atmospheric Pressure

M. Allen,* S. Davis,* W. Kessler,† H. Legner,* K. McManus,† P. Mulhall,‡ T. Parker,§ and D. Sonnenfroh†
Physical Sciences Inc., Andover, Massachusetts 01810

A combined experimental and analytical effort was conducted to demonstrate the applicability of OH Doppler-shifted fluorescence imaging of velocity distributions in supersonic combustion gases near and above atmospheric pressure. The experiments were conducted in the underexpanded exhaust flow from a 6.8-atm, 2400-K, H_2-O_2-N_2 burner exhausting into the atmosphere. The effects of pulse-to-pulse variations in the dye laser band shape and in-plane variations in temperature and pressure were examined in detail. A modification was developed to increase the single-pulse laser bandwidth, thereby increasing the intra-image velocity dynamic range as well as reducing the sensitivity of the velocity measurement to the gas property variations. Single-point and imaging measurements of the velocity field in the exhaust flowfield were compared with two-dimensional, finite-rate kinetics simulations of the flowfield. Relative velocity accuracies of ±50 m/s out of 1600 m/s were achieved in time-averaged imaging measurements of the flow over an order of magnitude variation in pressure and a factor of 2 variation in temperature.

Nomenclature

A = effective radiation rate
f_B = Boltzmann population fraction in absorbing state
$g_{(\omega)}$ = absorption line shape function
$I_{(\omega)}$ = laser spectral intensity
N_t = total number density of absorbing species
Q = effective quench rate
V_c = collection volume
η = transmissivity of collection optics
τ_p = laser pulse duration
Ω = collection solid angle

I. Introduction

INTEREST in supersonic propulsion systems (scramjets) and controlled hypersonic flight places new demands on experimental techniques for high-enthalpy combusting flow property measurements. Among the key parameters in combustor performance assessment is the vector velocity field throughout the propulsion system. Current velocity measurement techniques, such as hot-wire anemometry and laser-Doppler anemometry, are generally inapplicable in high-enthalpy, combusting supersonic flow test facilities or are subject to large systematic errors. The fluorescence approach investigated in this study circumvents many of the inherent limitations in conventional velocity measurement technology.

Other, nonintrusive, laser-based gas velocity measurement approaches have been the subject of intensive research and development in recent years. Approaches based on flow tagging have been demonstrated by several groups. Optical flow tagging approaches mark a line or a cross in the flow with one laser beam and then probe the marked line with a second laser beam or sheet at a known time later. The displacement of the marked gas during the known time delay gives the average convection speed during the time between the two laser pulses. This basic approach has been demonstrated using seeded biacetyl,[1] nascent molecular oxygen (RELIEF method),[2] and water vapor.[3,4] Water vapor tagging approaches use a tunable KrF excimer laser to dissociate H_2O into, among other products, ground state OH in a thin line along the laser beam. At some later time, a second laser is used to excite this OH line to record its displacement. In the RELIEF technique, gas marking is accomplished via Raman excitation of an excited vibrational level in the oxygen ground electronic state. Of these techniques, only the water vapor technique has promise for high temperature flows.

All flow-tagging velocity techniques, in effect, measure the convective velocity along a line in the flow which is averaged over the time between the marking and interrogating laser pulses. Thus, they find application primarily in flows whose principal mean velocity is nominally one dimensional. As long as the time delay between the two laser pulses is short compared to flow acceleration or eddy turnover time scales, this measured velocity is meaningful and turbulence statistics may be obtained.[5] Our focus in this work was the development of a velocity imaging technique which would permit two-dimensional velocity mapping in flows typical of practical high-speed combustion testing, i.e., H_2-air combustion gases with no seeding or diluents and no restrictions on flow dimensionality.

Elastic and inelastic scattering from molecules or particles illuminated by a sheet of laser light offer the potential for such velocity imaging. Velocity imaging techniques based on elastic scattering from particles[6] and molecules[7] have recently been demonstrated. In these techniques, the scattered light is Doppler shifted in frequency from the incident light and is imaged through ultra-narrow-band filters to provide velocity information. An alternative approach is to use inelastic scattering, or laser-induced fluorescence (LIF), to probe the Doppler shift of a molecular absorption feature. Relatively broadband fluorescence collection may then be used since the velocity information is encoded by the absorption process rather than by the detection filter. Numerous variations of this technique have been demonstrated and are reviewed subsequently. The goal of this study was to adapt Doppler-shifted fluorescence velocimetry to the constraints of practical high-speed combustor test facilities rather than to modify the gas or flow characteristics to improve the performance of the measurement technique. Relevant flows include undiluted H_2-air combustion gases with typical pressure variations from 0.5 to 5 atm and temperature variations from 1000 to 3000 K. Since these thermodynamic variations may not always be characterized simultaneously and may occur within the velocity measurement plane, we sought strategies to minimize their impact on the accuracy of the velocity determination. This paper reports the results of demonstration experiments in a representative H_2-air combustor using fluorescence from the nascent OH molecules in the reacting flow.

Presented as Paper 93-2032 at the AIAA/SAE/ASME/ASEE 29th Joint Propulsion Conference, Monterey, CA, June 28–30, 1993; received Sept. 28, 1993; revision received March 23, 1994; accepted for publication March 28, 1994. Copyright © 1994 by the American Institute of Aeronautics and Astronautics, Inc. All rights reserved.

*Principal Research Scientist. Member AIAA.
†Principal Scientist.
‡Senior Programmer.
§Principal Research Engineer. Member AIAA.

II. Overview of Doppler-Shifted Fluorescence Velocimetry

The magnitude of the fluorescence signal S_f recorded by an individual detector element is given by

$$S_F = \int_{\omega} I_{(\omega)}\, g_{(\omega)}\, d\omega \cdot \frac{A}{A+Q} \cdot (f_B V_c N_t) \cdot \left(\eta \frac{\Omega}{4\pi}\right) \cdot \tau_p \quad (1)$$

The first term in Eq. (1), the spectral overlap integral, is the velocity-sensitive term in the fluorescence equation.

The essence of LIF velocimetry is based on the Doppler-shifted absorption frequency of an ensemble of atoms or molecules. A group of molecules possessing a net directed velocity, when intersected by a laser beam traveling in a given direction, experiences an optical field which is Doppler shifted relative to an ensemble of stationary molecules. To first order, the magnitude of this Doppler shift is given by

$$\omega_v = \omega_0\left(1 - \frac{u}{c}\right) \quad (2)$$

where ω_0 is the zero-velocity absorption frequency, u the component of the gas velocity vector aligned with the laser propagation direction, and c the velocity of light.

The most direct measure of the magnitude of the Doppler shift is made by scanning a laser wavelength across an absorption line shape and determining the shift of the target line shape with respect to a stationary reference line shape. This approach was first suggested by Measures[8] and realized by Zimmerman and Miles.[9] A drawback to this approach, however, is the time required to complete a stable scan of the line shape. Recently, a modified ring-dye laser has been scanned across OH fluorescence line shapes in a supersonic reacting flow with an effective time resolution of approximately 1 ms for a single-point measurement.[10] Using a pulsed-dye amplifier, this approach has been extended to an imaging configuration,[11] although with much longer measurement times.

The scanned approach is, in principle, unnecessary. Since the magnitude of the spectral overlap integral depends on the relative frequency between the laser spectral intensity line shape and the molecular absorption line shape, it is possible to infer the relative velocity by a simple measure of the strength of the fluorescence signal, provided that the line shapes of the laser and absorber are accurately known. Of course, the fluorescence signal must also be normalized to account for variations in absorber number density, fluorescence efficiency, etc.

The form of the algorithm derived to determine the flow velocity from single-wavelength LIF measurements depends primarily on the dimensionality of the velocity field and the relative magnitude of the laser spectral bandwidth ($\Delta\omega_L$) and the molecular absorption bandwidth ($\Delta\omega_A$). Simple, closed-form expressions for the velocity as a function of the fluorescence signal can be derived by making assumptions regarding the relative width of the laser spectral bandwidth and the molecular absorption line shape $g_{(\omega)}$. References 12–14 have extensively examined the case where the laser spectral bandwidth is much narrower than the molecular absorption line shape. For this approach, the velocity may be determined using two fluorescence measurements from counter-propagating laser sheets S_{F^+} and S_{F^-}, where the ratio of the two measurements can be used to eliminate the signal dependence on the local OH number density. For narrow laser bandwidths, we obtain

$$V = \frac{c}{\omega_L}\left[\frac{2S_{F^+}}{S_{F^+}+S_{F^-}} - 1\right] g_{(\omega_L)} \Big/ \left(\frac{\partial g}{\partial \omega}\Big|_{\omega_L}\right) \quad (3)$$

In this case, the velocity algorithm is sensitive to the inverse of the slope of the molecular absorption line shape normalized by the magnitude of the line shape. This basic approach was extensively applied in the early LIF velocimetry literature using a frequency modulated Ar^+ laser and seeded iodine fluorescence. The velocity determined using this technique is sensitive to the local temperature and pressure, depending on the exact frequency of the laser relative to the molecular line shape center frequency.

The opposite limiting case is found when the laser spectral bandwidth is much larger than the molecular absorption line shape. Following an analogous approach to that used earlier, where the laser band shape is substituted for the absorption band shape, we derive

$$V = \frac{c}{\omega_L}\left[\frac{2S_{F^+}}{S_{F^+}+S_{F^-}} - 1\right] I_{(\omega_A)} \Big/ \left(\frac{\partial I}{\partial \omega}\Big|_{\omega_A}\right) \quad (4)$$

Equation (4) is similar to Eq. (3) except that the normalized line shape in the algorithm is now the laser line shape rather than the molecular absorption line shape. This is convenient since the algorithm is now independent of flow temperature and pressure fluctuations and is only a function of the laser spectral properties. This approach was used by Paul et al.[15] to measure the velocity distribution in a cold, supersonic jet seeded with NO. In this case, the low temperature and pressure of the flow collapsed the absorption line shape and a broadband pulsed dye laser was used to excite the fluorescence. This approach has also been recently pursued in high-temperature, low-pressure jets of NO and Ar (Ref. 16).

In the case of comparable laser and absorption bandwidths, analytical inversion of the fluorescence ratio in terms of velocity is only possible assuming a pure Gaussian (or Doppler broadened) absorption band shape. We instead define an implicit velocity algorithm

$$\Psi_{(u)} = \frac{2S_{F^+}}{S_{F^+}+S_{F^-}} - 1 = \frac{2S_{F^+}}{2S_{F^\pm}} - 1 \quad (5)$$

where $S_{F^\pm} = S_{F^+} + S_{F^-}$. For a planar laser-induced fluorescence (PLIF) experiment, this form may be preferred since one camera measures only S_{F^+} whereas the second camera can be configured to integrate both S_{F^+} and S_{F^-} (Ref. 15). This difference ratio is defined in the present application by analogy to the closed-form inversions derived for the narrow laser/absorption bandwidth cases discussed earlier and is applicable for any laser and absorption band shape. It is important to note that the difference ratio does not eliminate collisional-shift effects in the manner recently demonstrated for fully resolved, scanned line shape velocity imaging.[11] Indeed, counter-propagating beams cannot eliminate symmetric shift effects for single-wavelength velocity determinations.

Equation (5) is the form of the velocity algorithm used to reduce the fluorescence images to velocity distributions in this study. As discussed in detail in earlier publications,[17,18] both thermodynamic variations in the molecular absorption line shape and pulse-to-pulse variations in the laser spectral bandwidth can effect the velocity sensitivity of the algorithm defined by Eq. (5). To optimize the experimental configuration for OH velocimetry, detailed measurements of the OH (1, 0) band collisional broadening parameters were obtained for H_2-air gases as a function of stoichiometry and lower rotational level.[19] These measurements permitted the absorption line shape variations to be accurately predicted for typical temperature, pressure, and stoichiometry variations expected in a scramjet test environment.

III. Pulsed Dye Laser Band Shape Modifications

Spectrally resolved measurements of the single-pulse and multipulse average band shape of a Lambda-Physik FL3002 dye laser were reported previously.[17] These measurements, together with the OH line shape determinations, demonstrated that modification of the laser bandwidth is required to reduce the uncertainty in the velocity determination due to uncharacterized in-plane variations in the background temperature and pressure fields.

The bandwidth of the oscillator is related to the resolving power of the grating, neglecting the complexity of gain narrowing due to saturation and mode competition. This resolving power is proportional to the number of grooves illuminated by the oscillator beam. By inserting an intracavity aperture to reduce the image of the oscillator beam on the grating, we increased the bandwidth of the

radiation retroreflected back through the cavity. Since this bandwidth is an upper limit for the envelope under which the laser modes may oscillate, this technique increased the laser bandwidth.

The laser bandwidth was evaluated using an interferometer and the single-pulse monitoring setup described earlier.[17] We observed increasing laser bandwidth broadening as the aperture was reduced. Figure 1 is a comparison of the average visible laser bandshape in the standard configuration (solid line) to the average bandshape with half of the beam blocked (dashed line). The standard configuration average bandwidth is 0.15 cm^{-1} whereas the modified configuration is 0.24 cm^{-1}, a factor of 1.6 increase. This

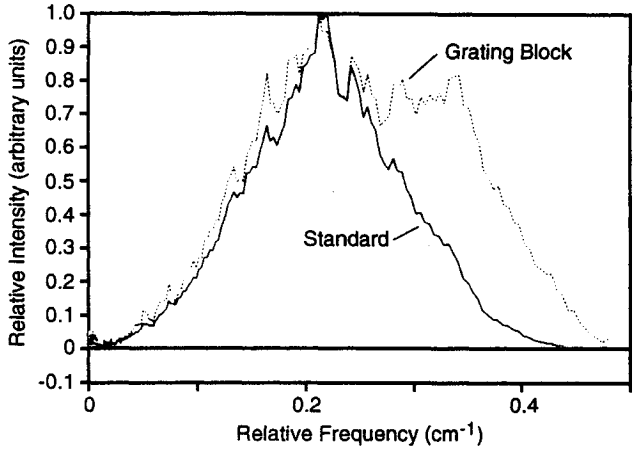

Fig. 1 Comparison of standard and modified average visible bandshape of FL-3002 dye laser. The laser wavelength was 565 nm and pulse energy was 25 mJ.

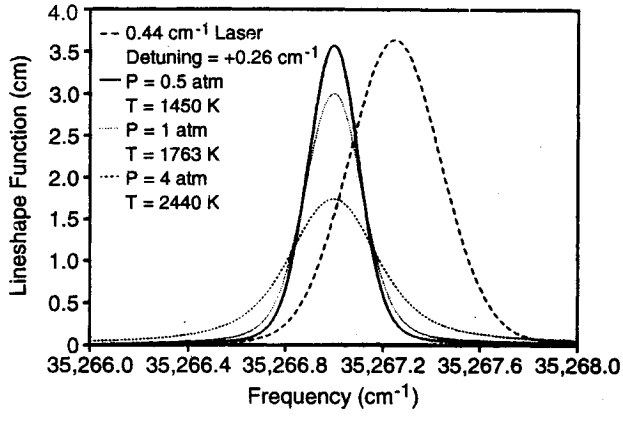

Fig. 2 Comparison of OH absorption line shapes at selected conditions in the jet flowfield with the uv laser bandshape.

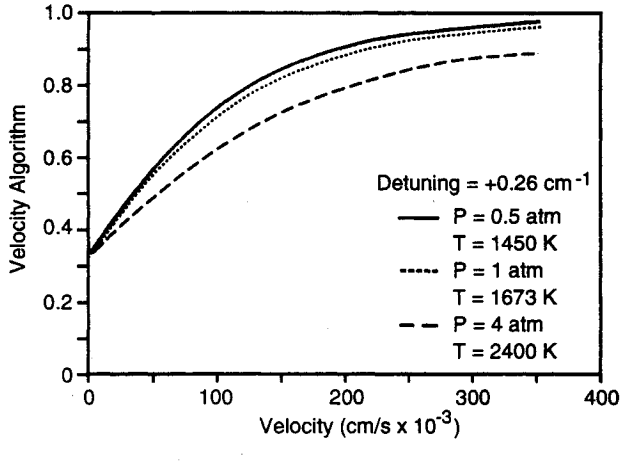

Fig. 3 Comparison of the velocity algorithm defined in Eq. (5) for typical thermodynamic flow.

Table 1 Reduced H_2-air chemistry model

No.	Reaction	Reaction Rate Variables A, cm^3/mole/s	n	E, cal/gmole
1	$H_2 + O_2 = OH + OH$	5.5×10^{13}	0	57,800
2	$H + O_2 = OH + O$	1.2×10^{17}	−0.91	16,500
3	$OH + H_2 = H_2O + H$	1×10^{8}	1.6	3,030
4	$O + H_2 = OH + H$	1.5×10^{7}	2.0	7,550
5	$OH + OH = H_2O + O$	3.4×10^{13}	0	5,020
6	$H_2O + H + OH = H_2O + H_2O$	1.4×10^{23}	−2.0	0
7	$N_2 + H + OH = H_2O + N_2$	2.2×10^{22}	−2.0	0
8	$H_2 + H_2O = H + H + H_2O$	3.3×10^{15}	0	96,000
9	$NO_2 + M = NO + O + M$	2×10^{16}	0	65,600
10	$NO_2 + H = NO + OH$	3.47×10^{14}	0	1,470

Table 2 Sonic jet inflow conditions

U, m/s	971.2
p, atm	4.0
T, K	2240
Species mass fractions:	
$f_1[H_2]$	1.669×10^{-4}
$f_2[O_2]$	3.175×10^{-2}
$f_3[H_2O]$	0.3142
$f_4[OH]$	3.456×10^{-3}
$f_5[H]$	6.582×10^{-6}
$f_6[O]$	1.778×10^{-4}
$f_7[NO]$	5.138×10^{-3}
$f_8[NO_2]$	5.895×10^{-6}
$f_9[N_2]$	0.6451

increase was accomplished with no loss of pulse energy. With the intracavity beam aperture, the single-pulse uv bandshape was measured to be between 0.35 and 0.55 cm^{-1} depending on the laser alignment.

Figure 2 summarizes the variation in the OH line shape over the range of typical thermodynamic conditions in this study. Also shown for reference is a uv laser band shape which is detuned +0.26 cm^{-1} from the zero-velocity line center and with a full-width at half-minimum of 0.44 cm^{-1}. The absorption line shapes were calculated using our measured broadening parameters and assuming equilibrium major species concentrations at the local temperature.[19] This magnitude of detuning is nearly optimal in minimizing the sensitivity of the velocimeter to the uncharacterized thermodynamic variations.

This is illustrated in Fig. 3, where we plot the velocity algorithm $\psi_{(v)}$ for the three conditions shown in Fig. 2. Except for the highest pressure condition, the curves lie close to one another, indicating a relative immunity to thermodynamic variations. The high-pressure curve corresponds only to conditions near the nozzle exit. Note that the curves do not collapse to zero at zero velocity. For this calculation we assumed that the forward propagating sheet had twice the energy of the rearward sheet. The effect of the unequal laser sheet intensities is to reduce the signal dynamic range of the measurement.

Modal fluctuations of the dye laser bandwidth were also examined in detail. As shown in Ref. 17, the effect of these variations for the frequency-doubled Lambda-Physik dye laser are generally smaller than the thermodynamic variations shown in Fig. 3 and can be neglected. This is consistent with similar results obtained by McMillin et al.[20] In lower pressure flows, where the velocity algorithm is more sensitive to the laser band shape, these modal fluctuations may constitute a significant source of error.

Figure 4 shows the effect of variations in the relative laser sheet intensity on the functional form of the velocity algorithm. In this case, the calculation was for P = 1 atm, T = 1673 K, and a static detuning of +0.18 cm^{-1}. The three curves shown span a range of I_B/I_F from 0.25 to 0.5. Variations in the relative sheet intensity across the two sheets were a much larger source of potential error than the uncharacterized variations in background gas temperature and pressure.

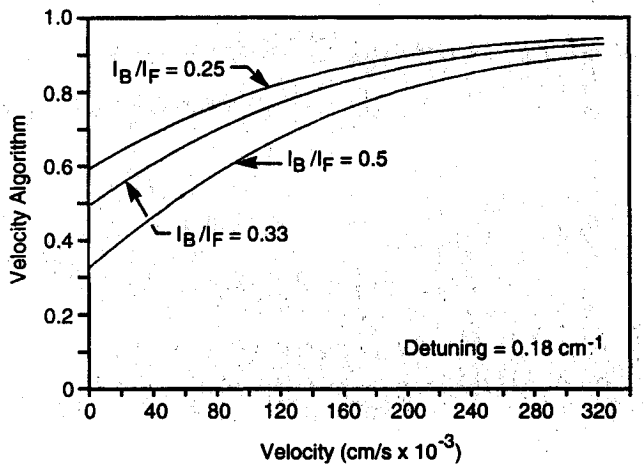

Fig. 4 Comparison of the velocity algorithm for various values of the relative sheet intensity.

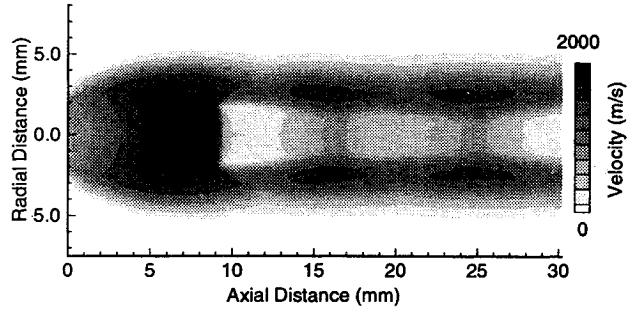

Fig. 5 Calculated axial velocity contours.

IV. Demonstration Flowfield

A. Supersonic Burner Overview

Development and optimization of the velocity imaging technique required a stable, continuous source of high-velocity gases at temperatures and pressures relevant to scramjet operation. An underexpanded supersonic jet flow with high-temperature, high-pressure stagnation conditions provided such a flowfield. We created these stagnation conditions using a high-pressure H_2-O_2-N_2 burner with a simple axisymmetric jet exhaust. The jet flow is reasonably well understood, both experimentally and analytically, and contains a wide range of velocity, pressure, and temperature variations in a small region downstream of the jet exit. These variations provide a stringent test of the technique's ability to determine gas velocity in the presence of large, uncharacterized in-plane property variations.

The body of the burner consisted of a 2-in. i.d. carbon steel pipe 6 in. in length surrounded by a press-fit copper jacket. Four sonic hydrogen injectors were located in the base, along with a spark ignitor and condensation drain. Four sonic, radial oxidizer jets were placed symmetrically around the burner one radius above the base. The oxygen/nitrogen ratio of the oxidizer was separately adjustable. Immediately above the oxidizer jets was a tap for a high-frequency pressure transducer. A static pressure tap was provided above the mounting yoke. A 70-deg interior taper nozzle, manufactured from Inconel 600, tapering to a 5-mm exit diameter, was clamped onto the end of the burner.

The burner body and nozzle were cooled using Dow-ThermA in a closed-loop heat exchanger. To reduce the heat transfer to the burner walls and to maintain the high gas enthalpy, a 2-in.-diam alumina tube wrapped with zirconia felt was fit into the burner. Stable combustion was achieved at the design pressure of 100 psi for extended periods (typically ~30 min). No significant instabilities were recorded either by the pressure transducer or by PLIF imaging of the OH distribution in the jet exhaust.

B. Jet Flow Simulations Using SPARK

To assess the accuracy of the velocity images, computational studies of the jet flows were performed using the SPARK code.[21] This code solves the compressible, Reynolds-averaged, Navier-Stokes equations including finite-rate chemistry for the important gas species found in these high-temperature jets.

Since the underexpanded jet flow consisted of recombining combustion product gases, we developed a reduced reaction mechanism for H_2-air chemistry based on consideration of more extensive mechanisms in the literature[22,23] and the flow residence times involved. Considerable simplification occurs by neglecting the ignition part of the problem. The reaction rate variables for this reduced set are given in Table 1. The exhaust gas at the nozzle exit was assumed to be in chemical equilibrium at the nozzle exit temperature. The initial jet conditions are summarized in Table 2. In the calculations, a small coflow of 3.5 m/s was imposed to sweep artificial pressure waves out of the computational domain.

Figure 5 shows the calculated axial velocity contour for the jet. Calculated pressure and temperature variations were used to assess the potential thermodynamic variations over which the velocity measurement would be made. Complete flowfield results are available in a separate report.[24] To verify the SPARK results and to confirm the operating conditions of the burner, we conducted series of scanned line shape velocity measurements along the burner centerline. Fluorescence line shapes were recorded simultaneously in the jet flowfield and in a low-velocity methane-air flame. The Doppler shift was determined from the two line shapes, after correction for pressure shifts.

The series of measurements are summarized in Fig. 6, where the mean velocity determinations are plotted against both the SPARK calculations and experimental correlations available in the literature (cf., Ref. 25 and the references therein). Except for the first data point at the jet throat, the measured velocity profile agrees well with the SPARK predictions. The low measured throat velocity was a persistent feature in several, repeated experiments and may be due to nonidealities in the throat flowfield due to boundary-layer effects.

V. Imaging Instrument Characterization Experiments

The experimental setup for the velocity imaging experiments is shown in Fig. 7. The uv and residual visible output from the laser were directed along separate paths. The uv beam was directed toward the burner, where an anti-reflection-coated beam splitter was used to create two beam paths. The primary, forward propagating beam was then formed into a thin sheet approximately 2 cm in height and 250-μm thick. This sheet was directed along the top of the burner. The second beam passed near the burner and traveled about 25 ft across the laboratory to a coated mirror, where it was retroreflected back through a series of sheet forming optics. This backward propagating beam was then focused to the same plane in the jet flowfield as the forward propagating sheet. We typically delivered about 1.5 mJ in the forward sheet and about 0.75 mJ in the backward sheet.

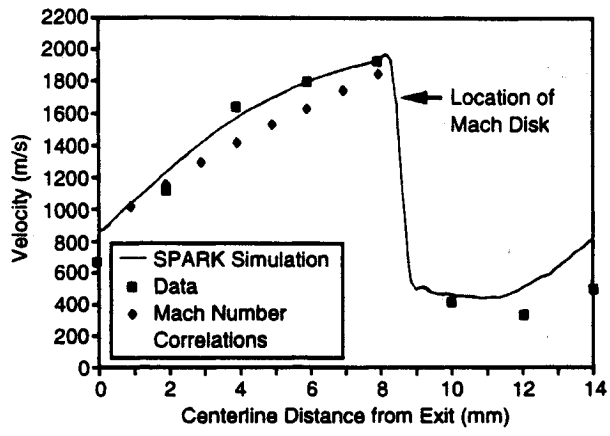

Fig. 6 Comparison of measured and calculated mean velocity profiles.

Two Phillips charge-coupled device cameras were used to image the fluorescence. One camera was fitted with a slow-gating intensifier ($\tau_{g,min} \sim 1$ μs) and the second with a fast-gating intensifier ($\tau_{g,min} \sim 20$ ns). The fast-gating tube used an additional layer of metalization on the photocathode which reduced the overall sensitivity of this camera by about an order of magnitude compared to the slow-gating camera. Prior to the experiment, both cameras are adjusted for minimum gain and offset variations across the array, thereby permitting a simple background subtraction to within the signal shot-noise limitations of the current data set. The two cameras were carefully aligned with an Air Force registration target prior to the experiments. To maximize the fluorescence collection efficiency, only 2-mm Schott Glass UG-5 blocking filters were used. These transmit over 90% of the fluorescence, but do little to reject scattered laser light or burner incandescence integrated by the slow-gating camera. For these reasons, we were unable to image the velocity closer than about 2 mm from the nozzle exit.

Example raw PLIF images obtained by excitation of the isolated $P_1(4)$ transition of the (1, 0) band at 283.463 nm are shown in Fig. 8. The right image is from the slow-gating camera which integrated both the forward and backward propagating laser sheets. The left image is from the fast-gating camera and is from the forward propagating sheet only. The burner is tilted at 56 deg from the vertical. The field of view in both images is 2.56 cm (H) by 1.92 cm (V) and the jet flow is from lower right to upper left. The signal level in each image has been rescaled for this figure so the gray scales do not represent the actual relative signal strengths between the two images. The slow-gating image at the left is the average of 24 laser pulses, and the fast-gating image at the right is the average of 12 laser shots.

The velocity sensitivity of the fluorescence signal is immediately apparent from the difference in the flow structure revealed by

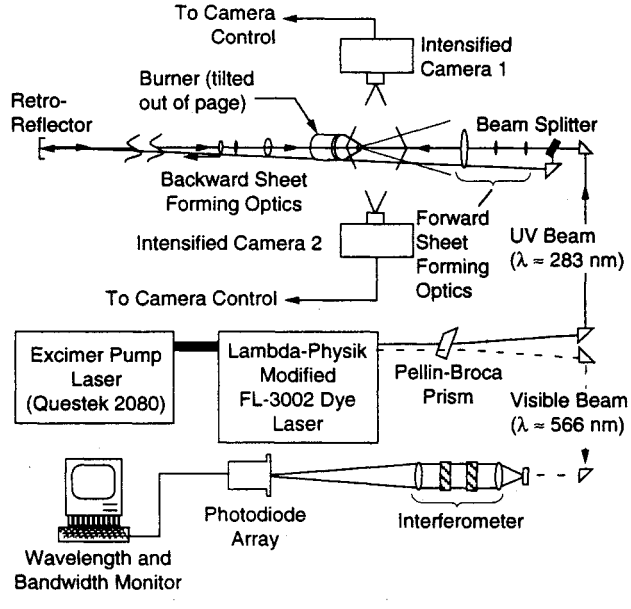

Fig. 7 Experimental configuration for velocity imaging demonstrations.

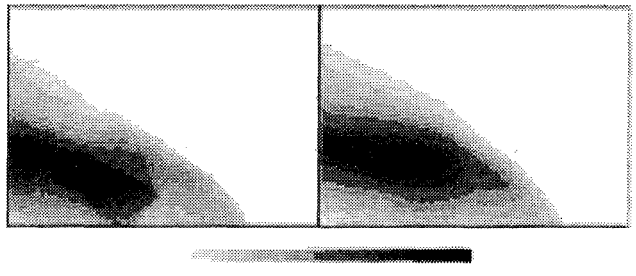

Fig. 8 Comparison of raw PLIF images from slow gating camera (right) and fast gating camera (left).

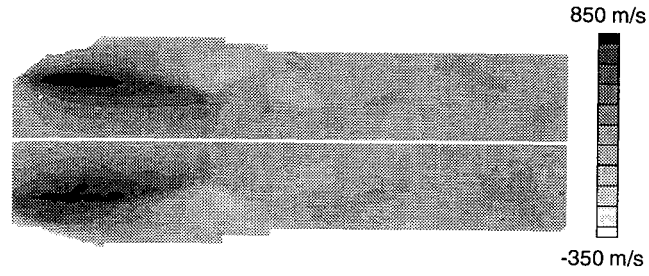

Fig. 9 Comparison of calculated (upper) and measured (lower) radial velocity distributions. Gray scale look-up-table units in m/s.

each image. For these images, the laser was detuned from the static absorption line center by +0.26 cm^{-1}, as determined by the shift in the interferogram recorded from the Fabry-Perot. This is near the half-power value of the unshifted convolution line shape. The slow-gating camera, integrating both forward and backward propagating sheets, averages both up- and down-shifted fluorescence signals, resulting in a fluorescence signal which is independent of velocity but which retains some pressure and temperature sensitivity from the absorption line shape near the half-width of the convolution profile. Most of the signal variations in the jet are due to variations in the laser sheet energy profile. The Mach disk is barely visible near the bottom of the image. The fast-gating camera, in contrast, views only the forward propagating sheet. Since we have already detuned the laser to higher frequencies, regions of high velocity in the flow are further shifted out on the convolution line shape, resulting in lower fluorescence signals. Thus, the left image in Fig. 8 has the highest fluorescence signals in the low velocity regions immediately downstream of the Mach disk.

Based on the SPARK prediction of ~0.5% OH (mole-fraction) at typical post-Mach disk conditions of ~1 atm and 2400 K, the available laser energy generated a signal level of approximately 1500 photons/pixel. For the 10% quantum efficiency of the slow-gating camera, this corresponds to a signal-to-noise ratio (SNR) of about 12. For the fast-gating camera, the lower quantum efficiency and the fact that only one sheet was used resulted in a single-pulse SNR of only about 4. By image averaging, we were able to improve this to about 10.

Since we anticipated potential errors due to variations in the relative laser sheet intensity distribution between the forward and backward propagating sheets, initial measurements were made using a single laser sheet and camera. The burner was directed vertically, so that only the radial velocity components of the jet could Doppler shift the absorption line shapes. This image was then mirrored about the axis of symmetry of the flowfield to synthesize the backward propagating sheet image. The images were then processed according to Eq. (5) using a single jet condition of 1 atm and 1700 K and scaled so that the zero velocity contour at the jet centerline was at the center of the dynamic range of the image. Since a single laser sheet was used to generate the two images, there is no variation in the relative laser sheet intensity, and we have introduced no velocity uncertainty due to this effect. Figure 9 is a comparison of the calculated radial velocity distribution to the measured velocity distribution. The measured velocity frame has been scaled to match the velocity range in the calculated frame. Since the algorithm of Eq. (5) is essentially a linear function of velocity over this range, the scaling is simply placing the relative velocity map on an absolute basis against the code predictions. The agreement between the calculated and measured velocity distributions is excellent through all regions of the near jet flowfield, including reversed flow regions.

From the nozzle exit at the bottom of the image, through the Mach disk, and extending to the end of the second shock cell, all of the major flow patterns are correctly visualized, despite the order of magnitude variation pressure and the factor of 2 variation in temperature. This agreements encompasses both the largely laminar flow in the jet core as well as the turbulent shear layers sur-

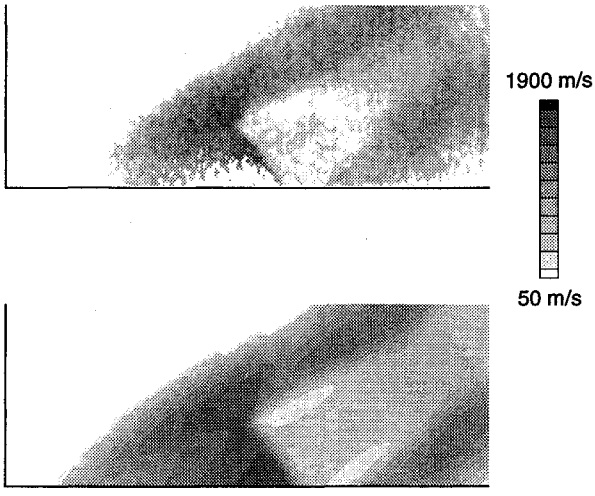

Fig. 10 Comparisons between measured (upper) and calculated (lower) angular velocity distribution. Gray scale look-up-table in units of m/s.

rounding the barrel shock and downstream of the triple point. Note that regions of the flow with velocity variations less than 100 m/s are clearly resolved. It is important to emphasize that the velocity data in Fig. 9 has not been corrected for any variations in pressure- or temperature-dependent broadening or shifting of the OH absorption line shapes. Because of the tailoring of the laser bandwidth and the selected value of the static detuning, the sensitivity of the velocity algorithm to the large variations in the flowfield has been reduced to near the residual shot-noise limit of the fluorescence data and can be ignored.

For flows without axes of symmetry or for single-pulse images, the two-camera/two-laser sheet approach is required. This type of measurement places much more stringent demands on the maintenance of constant, known relative laser sheet intensities. Fluorescence images were processed according to Eq. (5) and then scaled to the nonlinear velocity range using a model of the velocity dependence of the Doppler-shifted OH absorption line shape (at representative pressure and temperature) and the measured laser band shape. As with the radial velocity images, the absolute velocity range was obtained by scaling the maximum value of the velocity algorithm to the maximum velocity predicted by the SPARK simulations.

Figure 10 is a comparison of the velocity image obtained from the two-camera determination with the 56-deg velocity component calculated by the SPARK code. Despite the problems described with the relative laser sheet variations, the agreement between the measured and calculated velocity distributions is reasonable. Note that the white region below the Mach disk at the bottom center of the measured velocity image is due to lack of OH fluorescence signal there and does not represent an erroneous determination of low velocity. The region of high velocity near the triple point is also observed in the data, and relative velocity variations are in general correctly captured. Deviations between the measured and calculated velocity distributions near the top and bottom of the flowfield are attributable to the variations in the relative laser sheet intensity.

Since the two cameras used for this experiment used different gate-on times, another source of potential systematic error is introduced. This arises from the finite signal collected during the fluorescence decay after the laser pulse terminates. At the lowest pressure, lowest temperature portions of the jet flow, the characteristic fluorescence decay time is on the order of 5 ns, which, together with the nominal 15-ns laser pulse duration, suggests that the 20-ns gate on the fast-gating camera may not integrate the entire fluorescence pulse. The 1-μs gate used for the slow-gating camera, however, will integrate the entire pulse. For this flowfield, this effect is largely limited to regions of the flow below atmospheric pressure (i.e., the region immediately upstream of the Mach disk) and is estimated to introduce less than 10% uncertainty in the fluorescence ratio. For flows at lower pressures, it may be a more severe effect and suggests that cameras with identical and accurately timed intensifier gates should be employed.

VI. Discussion and Summary

Since the dominant source of error in the two-camera experiments arose from an experimental artifact (i.e., the uncorrected relative sheet energy distributions), it is not straightforward to determine a single figure of merit for the accuracy of the technique as demonstrated in these experiments. The single-camera demonstrations are free from the relative laser sheet intensity artifacts and are perhaps a better measure of the ultimate accuracy of the technique. In these images, the relative velocity uncertainty is on the order of ±50 m/s out of a total dynamic range of 1600 (-830 m/s $< u <$ 830 m/s), or about 3%. Here, the uncertainty is based on the smallest velocity variations recorded in the image. This uncertainty appears to be limited by the shot-noise statistics in the image rather than any systematic error due to the changing thermodynamic conditions in the flowfield. Of course, this low uncertainty has been achieved by averaging together 24 images. The single-shot uncertainty would be about 15% for these experimental conditions. Note that the axisymmetry of the jet is invoked only in the application of a single camera/laser sheet in the experimental setup. The flow symmetry in no way reduces the potential sensitivity of the measurement to in-plane temperature or pressure variations.

The angular velocity determinations have much larger shot-noise contributions. The velocity image from Fig. 10 was calculated using the average of 24 slow-gating camera images and 12 fast-gating camera images. The random velocity variation due to the shot noise is about ±200 m/s, or 12% of the total dynamic range. Systematic errors due to the variations in the relative laser sheet intensity increase this uncertainty near the edges of the laser sheets. Since the pulse energy for each PLIF image is less than half of that used in the radial velocity determination, the single-shot uncertainty is concomitantly higher. At these low energy levels the single-shot uncertainty of the fast-gating camera image approaches 40%. Attempts to calculate velocity images from selected single-pulse data were plagued by these large, random uncertainties which essentially masked most significant flow features.

In many applications, the frame averaging employed in these results may not prove burdensome, particularly since most computational fluid dynamics models of such flowfields are used to predict mean velocity distributions, as we have measured. As a result of the inherently low signal-to-noise ratio associated with PLIF imaging measurements in general, it is likely that image averaging will be used in most applications of Doppler-shifted velocity imaging where such averaging is possible. In future applications, it may be interesting to examine the effect of image averaging, particularly since the fluorescence signal is conditionally weighted on the presence of OH. In turbulent mixing layers, where the concentration of OH (or any other tracer species used to generate the fluorescence signal) is highly intermittent, the mean velocity determined by such averaging may be biased, as is the case in some laser Doppler velocimetry applications. Also, the effect of spatial averaging across the measurement volume (typically 50 × 20 × 500 μm in the present experiments) may bias the averaging in flows with significant variations at small scales. These caveats notwithstanding, the present results suggest that Doppler-shifted OH velocimetry can provide usefully accurate mean velocity data in flows where in-stream data was previously unavailable.

Improved accuracy in velocity mapping at these pressures, temperatures, and OH concentration levels requires more laser energy than was available from our pulsed dye laser. Pumping the dye laser with XeCl instead of XeF would approximately double the output pulse energy. Other pulsed dye laser systems, however, can produce 30–40 mJ at these wavelengths. These energy levels would permit true single-shot velocity imaging with acceptable uncertainties. Our examination of the Spectra-Physics PDL series dye lasers determined that their pulse-to-pulse spectral stability was not adequate for velocimetry applications. If single-shot velocity imaging is a stringent requirement, other dye lasers should

be explored to verify that their spectral stability is sufficient for velocimetry applications. Additional improvements could be obtained with higher quantum efficiency in the fast-gating camera.

Acknowledgments

Portions of this work were sponsored by the NASA Lewis Research Center and the Air Force Wright Laboratory. Robert Anderson, the NASA technical monitor, assisted in securing Cray computer time from NASA Lewis to support the SPARK modeling. John Smith, the Air Force technical monitor, assisted in review of the burner design. Erwin Lezberg and Ray Gaugler, also of NASA Lewis, consulted in the design of the supersonic burner and the heat transfer analysis of the nozzle. Phillip Paul, Sandia National Laboratory, and Berndt Nikolaus, Lambda-Physik, suggested possible laser band shape modification strategies. Our SPARK modeling efforts were enhanced by discussions with Hossein Haj-Hariri of the University of Virginia, as well as Dean Ecklund and Phillip Drummond of NASA Langley.

References

[1]Hiller, B., Booman, R. A., Hassa, C., and Hanson, R. K., "Velocity Visualization in Gas Flows Using Laser-Induced Phosphorescence of Biacetyl," *Review Science Instrumentation,* Vol. 55, No. 12, 1984, pp. 1964–1967.

[2]Miles, R. B., Connors, J. J., Markovitz, E. C., Howard, P. J., and Roth, G. J., "Instantaneous Profiles and Turbulence Statistics of Supersonic Free Shear Layers By Raman Excitation Plus Laser-Induced Electronic Fluorescence (RELIEF) Velocity Tagging of Oxygen," *Experiments in Fluids,* Vol. 8, 1989, pp. 17–24.

[3]Boedeker, L. R., "Velocity Measurement By H_2O Photolysis and Laser-Induced Fluorescence of OH," *Optical Letters,* Vol. 14, No. 10, 1989, pp. 473–475.

[4]Goss, L. P., Chen, T. H., Trump, D. D., Sarka, B., and Nejad, A. S., "Flow-Tagging Velocimetry Using UV-Photodissociation of Water Vapor," AIAA Paper 91-0355, Jan. 1991.

[5]Miles, R. B., Zhou, D., Zhang, B., Lempert, W. R., She, Z.-S., "Fundamental Turbulence Measurements by RELIEF Flow Tagging," *AIAA Journal,* Vol. 31, No. 3, 1993, pp. 447–452.

[6]Usry, J. W., Meyers, J. F., and Miller, L. S., "Doppler Global Velocimeter Measurements of the Vortical Flow Above a Thin Delta Wing," AIAA Paper 92-0005, Jan. 1992.

[7]Seasholtz, R. G., and Zupanc, F. J., "Spectrally Resolved Rayleigh Scattering Diagnostic for Hydrogen-Oxygen Rocket Plume Studies," AIAA Paper 91-0462, Jan. 1991.

[8]Measures, R. M., "Selective Excitation Spectroscopy and Some Possible Applications," *Journal of Applied Physics,* Vol. 39, 1968, p. 5232.

[9]Zimmerman, M., and Miles, R. B., "Hypersonic-Helium-Flowfield Measurements with the Resonant Doppler Velocimeter," *Applied Physics Letters,* Vol. 37, 1980, pp. 885–887.

[10]Chang, A. Y., Battles, B. E., and Hanson, R. K., "Simultaneous Measurements of Velocity, Temperature, and Pressure Using Rapid CW Wavelength-Modulation LIF of OH," *Optical Letters,* Vol. 15, No. 12, 1989, pp. 706–708.

[11]Klavuhn, K. G., Gauba, G., and McDaniel, J. C., "High-Resolution OH LIF Velocity Measurement Technique for High-Speed Reacting Flows," AIAA Paper 92-3422, July 1992.

[12]McDaniel, J. C., Hiller, B., and Hanson, R. K., "Simultaneous Multiple-Point Velocity Measurements Using Laser-Induced Iodine Fluorescence," *Optical Letters,* Vol. 8, No. 1, 1983, pp. 51–53.

[13]Hiller, B., McDaniel, J. C., Rea, E. C., Jr., and Hanson, R. K., "Laser-Induced Fluorescence Technique for Velocity Field Measurements in Subsonic Gas Flows," *Optical Letters,* Vol. 8, No. 9, 1983, pp. 474–476.

[14]Hiller, B., and Hanson, R. K., "Simultaneous Planar Measurements of Velocity and Pressure Fields in Gas Flows Using Laser-Induced Fluorescence," *Applied Optics,* Vol. 27, No. 1, 1988, pp. 33–48.

[15]Paul, P. H., Lee, M. P., and Hanson, R. K., "Molecular Velocity Imaging of Supersonic Flows Using Pulsed Planar Laser-Induced Fluorescence of NO," *Optical Letters,* Vol. 14, No. 9, 1989, pp. 417–419.

[16]Palmer, J. L., McMillin, B. K., and Hanson, R. K., "Planar Laser-Induced Fluorescence Imaging of Velocity and Temperature in Shock Tunnel Free Jet Flow," AIAA Paper 92-0767, Jan. 1992.

[17]Allen, M. G., Davis, S. J., Kessler, W. J., and Sonnenfroh, D. M., "Doppler-Shifted Fluorescence Imaging of Velocity Fields in Supersonic Reacting Flows," AIAA Paper 92-2964, July 1992.

[18]Paul, P. H., Seitzman, J. M., Lee, M. P., Palmer, J. L., and Hanson, R. K., "PLIF Imaging in Supersonic Flows," AIAA Paper 89-2912, July 1989.

[19]Kessler, W. J., Allen, M. G., and Davis, S. J., "Rotational Level-Dependent Collisional Broadening and Line Shift of the $A^2\Sigma^+$-$X^2\Pi$ (1, 0) Band of OH in Hydrogen-Air Combustion Gases," *Journal of Quantitative Spectroscopy and Radiative Transfer,* Vol. 49, No. 2, 1993, pp. 107–117.

[20]McMillin, B. K., Palmer, J. L., and Hanson, R. K., "Temporally Resolved, Two-Line Fluorescence Imaging of NO Temperature in a Transverse Jet in a Supersonic Cross Flow," *Applied Optics,* Vol. 32, No. 36, 1993, p. 7532.

[21]Carpenter, M. H., "Three Dimensional Computations of Cross-Flow Injection and Combustion in a Supersonic Flow," AIAA Paper 89-1870, July 1989.

[22]Sangiovanni, J. J., Barber, T. J., and Syed, S. A., "The Role of Hydrogen/Air Chemistry in Nozzle Performance Simulation for Hypersonic Propulsion Systems," AIAA Paper 90-2492, July 1990.

[23]Harradine, D., Lyman, J., Oldenborg, R., Schott, G., and Watanabe, H., "Hydrogen/Air Combustion Calculations: The Chemical Basis of Efficiency in Hypersonic Flows," AIAA Paper 88-2713, July 1988.

[24]Allen, M. G., Davis, S. J., Kessler, W. J., Legner, H. H., McManus, K. R., Mulhall, P. A., Parker, T. E., and Sonnenfroh, D. M., "Instantaneous Velocity Field Imaging Instrument for Supersonic Reacting Flows," Final Rept. NASA Contract NAS3-25790, NASA CR 191162, Sept. 1993.

[25]Ewan, B. C. R., and Moodie, K., "Structure and Velocity Measurements in Underexpanded Jets," *Combustion Science and Technology,* Vol. 45, 1986, pp. 275–288.